Energetics and mechanical properties of silica nanotubes

2007 J. Phys.: Condens. Matter 19 386238

(http://iopscience.iop.org/0953-8984/19/38/386238)

IOP PUBLISHING JOURNAL OF PHYSICS: CONDENSED MATTER

J. Phys.: Condens. Matter **19** (2007) 386238 (25pp) doi:10.1088/0953-8984/19/38/386238

Energetics and mechanical properties of silica nanotubes

Krishna Muralidharan[1,2], **Juan Torras**[1,3,4] **and S B Trickey**[1]

[1] Quantum Theory Project, Departments of Physics and of Chemistry, University of Florida, Gainesville, FL 32611-8435, USA
[2] Department of Materials Science and Engineering, University of Arizona, Tucson, AZ 85721, USA
[3] Departament d'enginyeria Química, EUETII, Universitat Politècnica de Catalunya, Plaça del Rei 15, 08700-Igualada, Spain

E-mail: torras@euetii.upc.edu

Received 6 June 2007, in final form 9 August 2007
Published 6 September 2007
Online at stacks.iop.org/JPhysCM/19/386238

Abstract

The energetically favorable structures and mechanical response to tensile and pure bending forces of single-wall and multi-wall cylindrical silica nanotubes of varying lengths and radii are predicted via classical molecular dynamics and checked, in part, by quantum mechanical studies. Two distinct parameterizations of a popular pair potential are used. One is adapted to bulk properties, the other to small nanoclusters. Predicted stable structures for single-walled tubes as a function of length at specified radii are dependent on potential parameterization. For the bulk-adapted parameterization, single-walled tubes with large radii (12-membered rings) have an energetic preference to rearrangement into twinned parallel-column structures. Conversely, the nanobased parameterization puts such twinned structures slightly higher in energy than the corresponding single tubes. Both the mechanical properties and failure mechanisms in tension and pure bending of the single-walled tubes depend upon the nanorod dimensions. Predicted structures for the double-walled nanotubes exhibit qualitatively opposite trends for the two parameterizations. Though the potentials give different values for the tensile and bending elastic moduli for the various structures, the qualitative pictures of nanotube failure are quite similar. For comparison and insight, we also studied a small single-walled nanotube using both pure quantum forces and quantum–classical multi-scale simulations. Some distinctly different behaviors emerged.

[4] Author to whom any correspondence should be addressed.

1. Introduction

Silica nanostructures have been the subject of recent theoretical [1–3] and experimental studies because of the potential importance of such structures for photonics, electronics, pharmaceuticals, and catalysis [4–9]. Particular attention has been paid to silica nanotubes, given their structural similarity to carbon nanotubes, which in turn, have been under immense scrutiny in the last decade. Since the work of Nemetschek and Hofmann [10], there have been many efforts to form silica nanotubes using biological substrates, carbon nanotubes, nanomembranes, and metal oxides as templates [11–15]. Yet not much seems to be known about the energetics and mechanical properties of such nanostructures. Thus, we examine the properties of silica nanotubes that have initial axial symmetry and consist of stacked silica rings with even numbers of silica units. Specifically, we look at the relative energetic stabilities of such nanotubes and a related multi-wall nanotube as a function of ring size and tube length. Further, we examine the behavior of the nanotubes under pure tension or bending. For comparison and insight, we also examine the structure and mechanical properties of a relatively small silica nanotube as predicted by both multi-scale, quantum mechanical and all-quantum force calculations.

2. Methodology

2.1. Nanotube construction

The structure of all the silica nanotubes under study is similar to the model nanorod that Zhu *et al* constructed for investigation of hydrolytic weakening in silica systems [16]. Their nanorod consisted of eight six-membered planar silica rings connected via bridging oxygens and terminated with oxygen atoms at both ends so as to preserve stoichiometry. We denote this single-walled tube (SWT) structure as $6M$–$8L$ (six-membered rings, eight rings long). The geometry provides a convenient model of the experimentally synthesized silica nanotube structures without introducing complications from terminating ligands. With that nanorod as a template, we constructed (i) tubes of varying radii by adding or removing Si (and corresponding O) atoms in a ring, and (ii) tubes of various lengths. Specifically we treated nanotubes of radii $4M$, $6M$, $8M$, $10M$, and $12M$ and lengths $6L$, $12L$, $18L$, $24L$, $30L$, and $36L$. The structure denoted as $6M$–$6L$ is shown in figure 1. In addition, we constructed multi-wall nanotubes (MWT) consisting of a $4M$ or $6M$ tube axially concentric inside a $10M$ or $12M$ SWT, all at different lengths.

2.2. Computational procedure

In any molecular dynamics (MD) simulation the inter-atomic potential determines the accuracy of the predicted thermodynamic and kinetic properties. Most successful potentials for silica are parameterized, at least in part, to reproduce the properties of bulk polymorphs of silica, hence might not be expected to model nanoscale structures accurately. The key issue is whether a classical potential can be adjusted so as to reproduce the quantum size effects characteristic of nanostructures. Toward that goal, there are potentials specifically parameterized to describe silica nanostructures. Therefore we employed both a nanoscale parameterization (hereafter FB [17]) and a bulk parameterization (hereafter BKS [18]) of the same functional form. While BKS incorporates both first-principles cluster and experimental bulk (quartz) information, FB is parameterized solely to yield the correct first-principles geometries and energies of some small silica nanoclusters. As a result, the two parameter sets are rather different. The

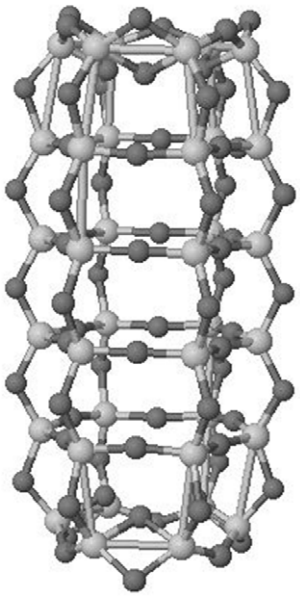

Figure 1. Six (6-L) six-membered (6-M) planar silica ring single-wall nanotube (6M–6L SWT); light grey spheres are Si atoms, dark grey O atoms.

Table 1. Parameter values for BKS, FB, and NTH-2 potentials. Charges Q in units of electron charge magnitude.

	i–j	A_{ij} (eV)	ρ_{ij} (Å)	C_{ij} (Å^{-6} eV)	Q_{Si}	Q_{O}
BKS	Si–O	18 003.757	0.205	133.538		
	O–O	1 388.773	0.362	175.000	2.400	−1.200
	Si–Si	—	—	—		
FB	Si–O	10 454.202	0.208	63.047		
	O–O	1 428.406	0.358	41.374	2.400	−1.200
	Si–Si	79 502.113	0.201	446.780		
NTH-2	Si–O	240 101.90	0.1270	2.0551		
	O–O	39 439.87	0.2147	5.8512	2.050	−1.025
	Si–Si	27 530.45	0.0467	1.5505		

functional form is

$$U(r_{ij}) = \frac{Q_i Q_j}{r_{ij}} + A_{ij} \mathrm{e}^{-\frac{r_{ij}}{\rho_{ij}}} - \frac{C_{ij}}{r_{ij}^6}. \tag{1}$$

Parameter values are given in table 1 (we discuss the NTH-2 parameterization also given in table 1 later). For the purely classical MD, we used the DL_POLY code [19]. To characterize the structure and energetics of the SWTs and MWTs for both the BKS and FB parameterizations, all structures initially were energy minimized at 0 K using the BFGS algorithm [20], then equilibrated at 10 and 300 K using the Nosé–Hoover thermostat. The binding energy/atom (BE) and the structural properties of the equilibrated nanotubes at 10 K then were determined as a function of tube dimensions; see section 3.

Tensile and bending properties of the equilibrated structures were studied for two methods of strain application; (i) displacement of end-cap atoms (comprising the end-ring Si atoms and

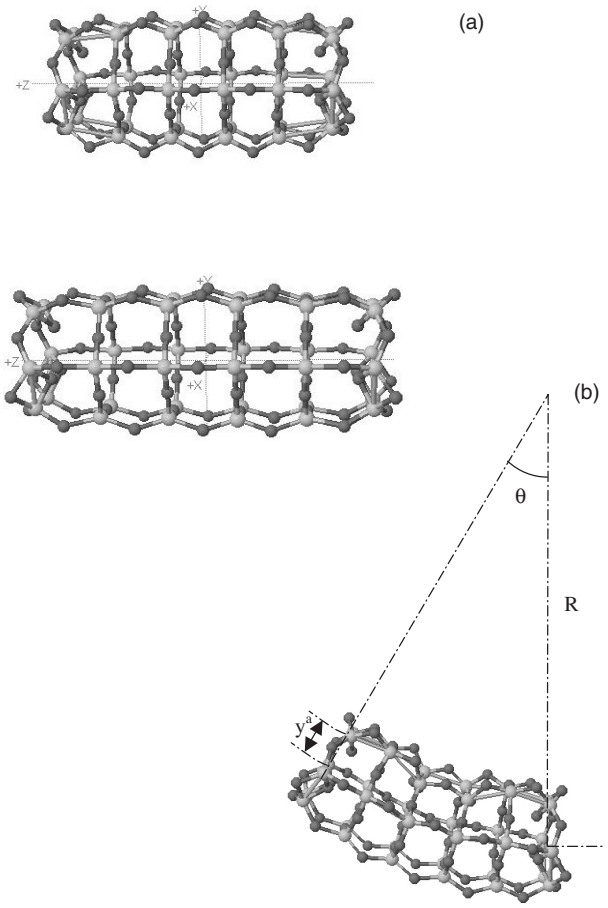

Figure 2. $6M$–$6L$ SWT: (a) under proportional tensile strain (PS) at two different simulation times, (b) under bending stress with curvature radius R and radial distance, y^a, to the central surface.

the O atoms attached only to those end-ring silicons) parallel to the principle (symmetry) axis at a velocity corresponding to a given strain rate with the other atoms unconstrained, and (ii) displacement of all atoms along the principle axis with the displacement proportional to the atom distance from the system center (see figure 2(a)) and velocity corresponding to a given strain rate. For brevity, we refer to the former procedure as end-atom strain (EAS) and the latter as proportional strain (PS). In both cases, the tensile strain is the ratio between the incremental deformation length of the system and the non-deformed length, $(L-L_0)/L_0$ and is incremented at each MD step according to the specified strain rate. The stress is obtained as the sum of the end-cap atom force components parallel to the symmetry axis divided by the projected cross sectional area of the end caps [21, 22]. Note that, in both types of tensile simulations, only the end-cap radii are kept fixed.

For bending the procedure was similar. The nanotubes were subjected to constant strain rates, with the strain applied via EAS, except, of course that the end-cap atom displacements were essentially radial; see figure 2(b). The opposite end of the nanotube was fixed (pinned). We assumed a quasi-cylindrical geometry for all systems (see figure 2(b)) with curvature radius R and radial distances y^a measured from the central axis. More precisely, y^a denotes the

perpendicular distance from the central surface, over which there is no stress. In an ideal homogeneous rod, the axial strain s_{y^a} at any y^a would be

$$s_{y^a} = \frac{y^a}{R} = \kappa y^a, \tag{2}$$

(κ = curvature). Adaptation of this definition to the atomistic rods under consideration requires specification of physically meaningful values of y^a. As in the stretching simulations, the end-cap radii were fixed. Denote that value as $y^a_{\max}$. From equation (2), the bending strain s_{y^a} at the end-caps is

$$s^{\max}_{y^a} = \kappa y^a_{\max}. \tag{3}$$

The torque on the system due to 'axial' forces (i.e., those forces normal to the plane of the end-cap Si atoms; see figure 2(b)) is

$$\mathcal{M} = \int F^a \, \mathrm{d}y^a = \int \sigma^{\mathrm{a}} y^a \, \mathrm{d}A, \tag{4}$$

where σ^{a} is the axial stress. Then, assuming the axial stress to be proportional to radial position,

$$\frac{\sigma^{\mathrm{a}}_{\max}}{y^a_{\max}} = \frac{\sigma^{\mathrm{a}}}{y^a}, \tag{5}$$

the torque becomes

$$\mathcal{M} = \frac{\sigma^{\mathrm{a}}_{\max}}{y^a_{\max}} \int (y^a)^2 \, \mathrm{d}A = \frac{\sigma^{\mathrm{a}}_{\max}}{y^a_{\max}} I, \tag{6}$$

so

$$\sigma^{\mathrm{a}}_{\max} = \frac{\mathcal{M}}{I} y^a_{\max}. \tag{7}$$

Here I is the areal analogue of a moment of inertia. At a given strain value, M was calculated as the sum of torques of the parallel components (with respect to the principal axis) of the end-cap atom forces, while I was taken as a constant in terms of $y^a_{\max}$.

The importance of quantum effects in nanostructures makes quantum mechanical benchmarking significant for any classical MD study such as this one. In principle one wants, at least, the Born–Oppenheimer potential energy surface instead of a model potential such as equation (1). The well-known difficulty is the extremely high computational cost–benefit ratio of even relatively simple quantum mechanical (QM) methods such as density functional theory (DFT), the Hartree–Fock (HF) approximation, or even tight-binding versions of them. For the larger systems in this study, the computational cost would be prohibitive. However, we did investigate the mechanical properties of a small system, the $6M$–$6L$ nanotube, under tension and bending using (i) a re-parameterized [23] semi-empirical QM method (MNDO [24]) and (ii) the multi-scale methodology of Mallik *et al* [22]. The multi-scale calculation involves the calculation of forces on atoms using either MNDO or a classical potential of the same form as FB and BKS, depending on whether the atoms are identified as 'quantum' or 'classical'. The potential parameterization differs from both FB and BKS values; see table 1. That parameterization, designated NTH-2 by its originators, was constrained specifically to match the MNDO stress response for the $6M$–$6L$ nanorod for uniaxial tensile strains up to 10%. We used the same semi-empirical MNDO97 program [24] with the NDDO parameters obtained via the transfer Hamiltonian method [23]. Automated interoperation of the MNDO97 code with the DL_POLY MD package [19] for these multi-scale simulations was achieved via the PUPIL framework [25, 26].

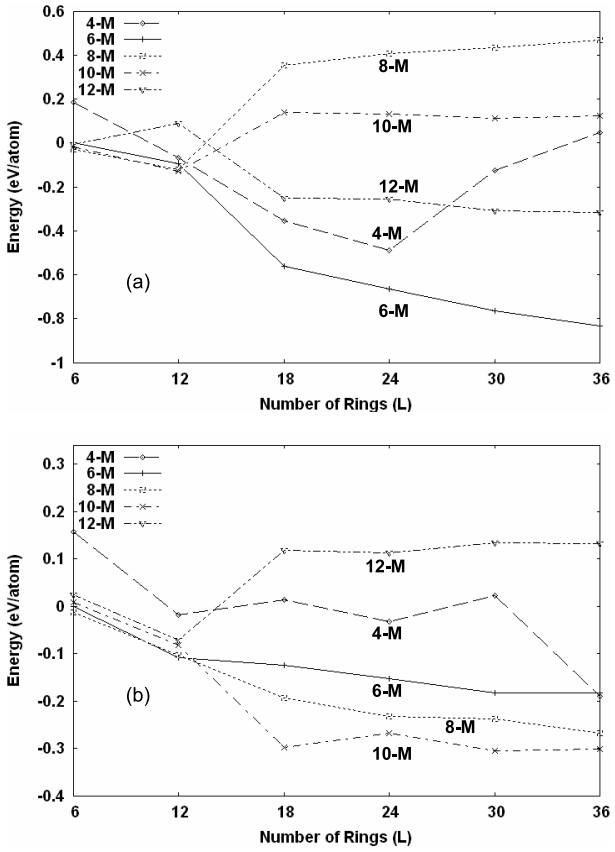

Figure 3. Variation in binding energies of SWT for different radii as a function of number of rings for (a) FB and (b) BKS. The energies are expressed with respect to the $6M$–$6L$ structures; see text.

3. Results and discussions

3.1. SWT equilibrium structures

Figures 3(a) and (b) present the variation in binding energy (BE) of the SWTs as a function of tube length (L) for different ring sizes (M) using the FB and BKS parameterizations respectively for equilibrium structures at $T = 0$ K. Those BE shifts are relative to the BE of the $6M$–$6L$ structure, -16.54 eV/atom for FB and -18.88 eV/atom for BKS. Those values, in turn, are with respect to the separated atom limit for the respective parameterizations. Notice that both those BEs are much larger in magnitude than the experimental BE of quartz (-6.4 eV/atom), a direct consequence of the potential parameterizations. Neither FB nor BKS was calibrated to match the absolute energies predicted by underlying quantum mechanical methods. For BKS, the parameters which yield the right ground state structure of α-quartz were chosen from among the multiple parameter sets that fit HF data on a tetrahedral cluster. The FB parameterization criterion was that the potential yield the right relative ordering of the DFT energetics of selected nanostructures.

Figure 3 shows that for the shorter FB SWTs, $L \leqslant 12$, the BEs of the $6M$, $8M$, and $10M$ structures are almost degenerate and lower than the corresponding BEs of the $12M$ and $4M$ structures. For $L > 12$, the FB $6M$ SWT structures are the most stable and appear to be

on a smooth progression to an extended system limit. On the other hand, the $4M$, $8M$, and $10M$ FB SWTs have energetically favored lengths ($L = 24$, 12, 12 respectively), suggestive perhaps of some systematic behavior ('magic number'). No trend toward a finite BE extended system limit is evident for the $4M$, $6M$, and $8M$ SWTs. Both the $10M$ and $12M$ FB SWTs are almost indifferent, so far as BE is concerned, to length beyond $18L$, suggestive of a rather weak progression to a finite BE infinite-length limit. Thus the FB parameter set, which is calibrated to small nanostructures, does display size effects for some but not all of these silica nanotubes.

The BKS SWTs differ, qualitatively and quantitatively, from the FB SWTs. Only the $12M$ BKS SWTs have an energetically favored length ($12L$). For $L > 12$, the $10M$ BKS structure is the most stable but only modestly so compared to the $8M$ systems. In marked contrast, at the same lengths those are the two *least* favorable FB structures. Both the $10M$ and $12M$ BKS SWTs exhibit insensitivity to length at large L, while the $6M$ and $8M$ BEs are only moderately sensitive to L. At large L, the $12M$ BKS systems are least favorable, in contrast to the FB prediction of being next-to-most favorable. Except for the $4M$, the BE dependence on L of all the BKS SWTs is suggestive of finite BEs in the infinite-length limit. Such behavior is at least consistent with the idea that the BKS parameterization cannot recognize nanoscale properties because that parameterization ultimately is determined by bulk silica properties.

The $4M$ systems thus are particularly interesting. For $L > 30$, the $4M$ BKS nanotubes are more favorable with respect to the shorter ones whereas the FB SWTs have the opposite energetics. For both parameterizations, when the systems were equilibrated at either 10 or 300 K, the longer $4M$ structures, namely the $30L$ and $36L$ for both parameterizations as well as the FB $4M$–$24L$ structure lost their tubular character and spontaneously twisted. See figure 4(a). Therefore, we do not report stress–strain results (see below) for $4M$ BKS systems with $L \geqslant 30$ nor FB systems with $L \geqslant 24$. Further, the fact that both parameterizations gave the same sort of geometry but opposite trends of energy with length is a striking example of parameterization sensitivity, one which should be quite testable. With two other exceptions, all the remaining SWTs retained their tubular structure when equilibrated at higher temperatures.

Those exceptions are the BKS $12M$–$6L$ and $12M$–$12L$ structures, which rearrange to form twin-columnar structures; see figures 4(b) and (c). A surprising structural feature of these twin-columnar structures is the presence of three-coordinated oxygens (3-C O) that connect the two columns, along with singly coordinated oxygens (1-C O) at the ends. For the FB parameterization, we did not see the spontaneous rearrangement of the $12M$–$6L$ and $12M$–$12L$ SWTs to form the twin-columnar structures when we equilibrated the structures at either 10 or 300 K. However, when initially placed in the twin-columnar structures, the FB systems did reach an energy minimum at $T = 0$ K and did retain that conformation at $T = 10$, 300 K. The BEs of the resulting two FB twin structures are higher than the corresponding single-wall tubes by only about 0.02 eV/atom: the two conformations are almost isoenergetic in the FB parameterization. Above $T = 0$ K, the absence of knowledge of entropic effects means that the energy differences just discussed must be interpreted with care. Nevertheless, there does seem to be strong indication of rearrangement being favored by the shorter $12M$ systems.

Returning to the topic of nanoscale versus bulk parameterization effects, it is illuminating to compare the BE of pairs of nanotubes with the same number of atoms. We considered three pairs: (i) $6M$–$8L$, $8M$–$6L$, (ii) $6M$–$10L$, $10M$–$6L$, and (iii) $6M$–$12L$, $12M$–$6L$ with 144, 180 and 216 atoms respectively. See table 2. For both parameterizations the $6M$ nanotubes always are lower in energy than their equal-population counterparts. This result might not seem to be too surprising given that bulk silica polymorphs are characterized by $6M$ rings. Still, the fact that, for a given length, the BKS BEs for $6M$ ring structures are higher than those of the $8M$ and $10M$ structures while FB favors the $6M$ structures for $\geqslant 12$ is rather striking since the FB parameterization has no input from bulk silica data, while BKS does. Moreover, there is a clear,

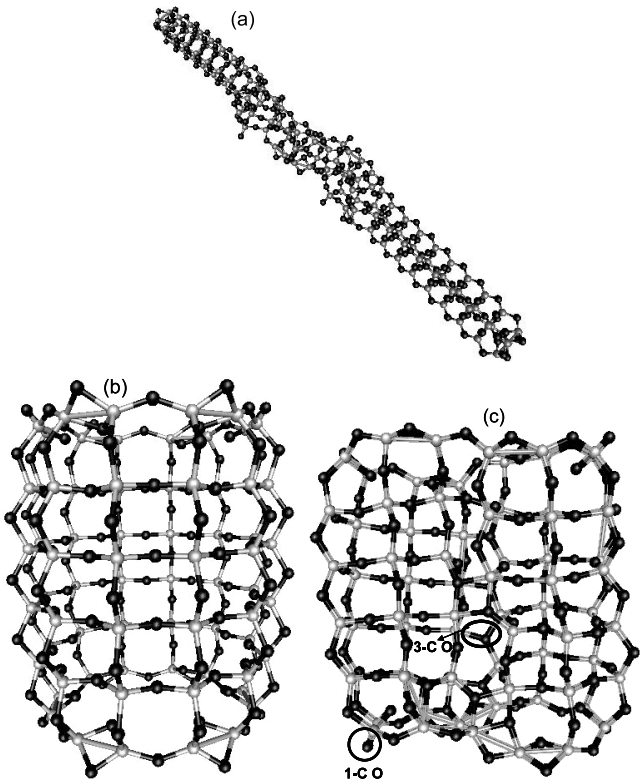

Figure 4. Structural illustration of (a) $4M$–$24L$ nanotube showing distortion from regular structure (see text), (b) $12M$–$6L$ nanotube, (c) $12M$–$6L$ twin-columnar nanotube. Oxygen and silicon atoms are represented by black and grey spheres respectively. One- and three-coordinated oxygens are encircled.

Table 2. Comparison of energies of different sized nanotubes having the same number of atoms. Energies are expressed with respect to the $6M$–$6L$ BE; see text.

	144		180		216	
	$6M$–$8L$	$8M$–$6L$	$6M$–$10L$	$10M$–$6L$	$6M$–$12L$	$12M$–$6L$
	(eV/SiO_2)		(eV/SiO_2)		(eV/SiO_2)	
FB	−0.05	−0.03	−0.07	−0.02	−0.10	−0.01
BKS	−0.05	−0.01	−0.08	0.01	−0.11	0.02

sharp distinction *for both parameterizations* between size as measured by SiO_2 population and as measured by the numbers of M and L.

Next we consider the $T = 10$ K structural characteristics of the various energy-minimized SWTs. For each SWT, we examined the average (i) inter-ring distances (R–R), (ii) intra-ring Si–O bond distances (R1), (iii) intra-ring Si–O–Si angles (A1), and (iv) bridging angles (A2), i.e. the angles formed between the Si–O bonds associated with the bridging oxygens. For clarity, all these quantities are illustrated in figure 5. Variations in these quantities as a function of L and M for both FB and BKS are displayed in figures 6 and 7 respectively. In each of those figures, the inset presents the corresponding end-cap structural quantity, in recognition of

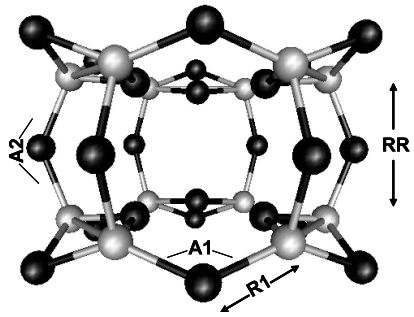

Figure 5. Representation of the structural quantities that characterize a nanotube, illustrated, for convenience, by the $6M$–$2L$ SWT. Oxygen and silicon atoms are represented by black and grey spheres respectively.

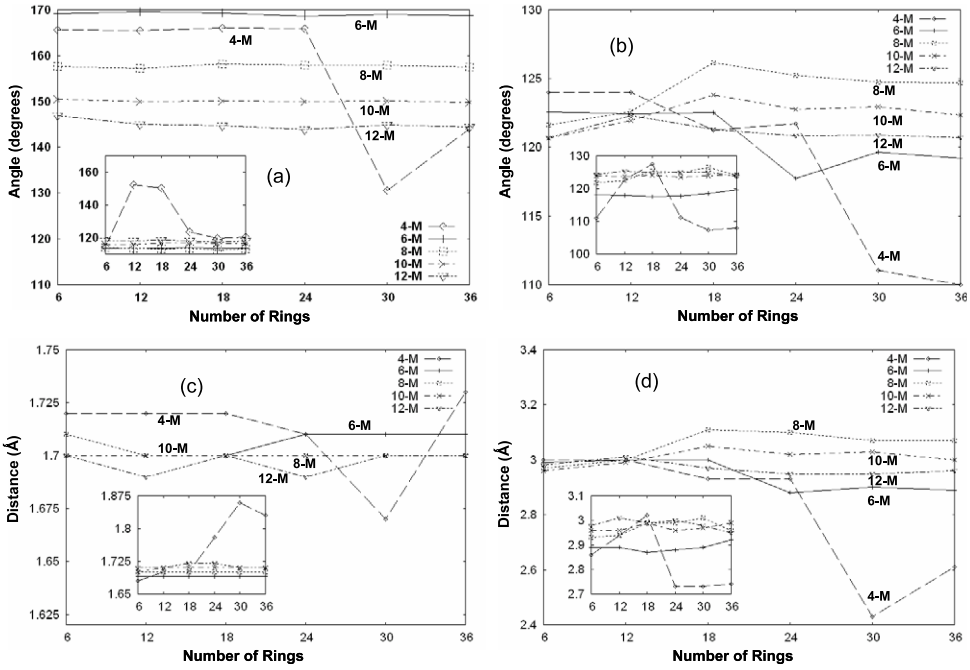

Figure 6. Variation of (a) A1, (b) A2, (c) R1, (d) R–R for the FB SWTs. The inset in each figure represents the corresponding end-cap structural quantities.

the fact that the end structure of all the SWTs differs from the rest of the tube because of the stoichiometry-preserving oxygen termination at the ends. In all structures, the intra-ring Si–O–Si angle typically equals the tetrahedral angle (109.5°). Among the rods, all the intra-ring Si–O–Si angles are rather similar and so also are the A2 values.

Examination of figures 6 and 7 reveals that, for both parameterizations, the variation in A1, A2, R1, and R–R with L for the longer ($L \geqslant 24$) $4M$ SWT structures differs greatly from the corresponding variations for the other tubes. The difference is attributable to the distorted nature of the equilibrated structures of the longer $4M$ tubes discussed above. Another striking fact is that for all but one of the SWTs, the FB R–R values are greater than those from BKS and consequently the FB tubes always are longer than the corresponding BKS tubes. The exception

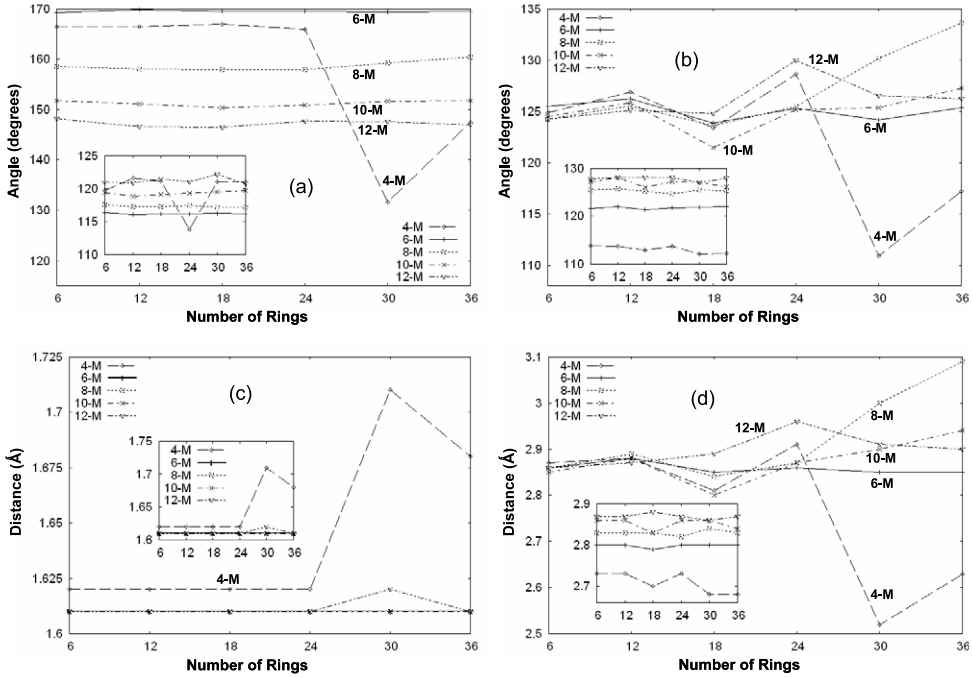

Figure 7. As in figure 6 for BKS SWTs.

is the case of large L for the $8M$ tubes for which the R–R values are similar. Also note that, except for $M = 4$, the FB systems exhibit much smoother L-dependence than the BKS systems. It remains to be determined (via multi-scale or all-quantum force calculations) whether this is a genuine size effect, as might be suggested by the FB parameterization procedure.

There are more subtle structural aspects of the various SWTs. Except for the $4M$ structures, the variation of A1 with L is very similar for both FB and BKS: A1 is almost independent of L and decreases with increasing M. There is no corresponding simple dependence of A2 upon M or L, though the values of A2 for both parameterizations are roughly comparable at all L (A2 $\approx 125°$). R1 values for the BKS tubes always are smaller than for the FB tubes, behavior that is consistent with that of R–R. Both behaviors are plausible, in that the BKS parameters were optimized to yield the ground state structure of quartz, which has a Si–O bond length $\approx$1.62 Å, while FB parameters were constrained to yield the calculated properties of silica nanostructures with typical bond lengths $\approx$1.68 Å.

3.2. MWT equilibrium structures

The multi-wall tubes (MWT) were formed by concentric nesting of $4M$ and $6M$ tubes within $10M$ and $12M$ tubes for different lengths, followed by relaxation at $T = 0$ K. The most stable (by about 0.05 eV/atom) among the various MWTs was the $6M$ nested within the $12M$ structures, referred to as the (12–6)M (see figure 8). It is the only one which we examine in more detail.

The variation in BE for the (12–6)M MWT as a function of L for both parameterizations is shown in figures 9(a) and (b) respectively. Those figures include, for comparison, the BEs of the SWTs that are the most favored energetically ($6M$ and $10M$ for FB and BKS respectively).

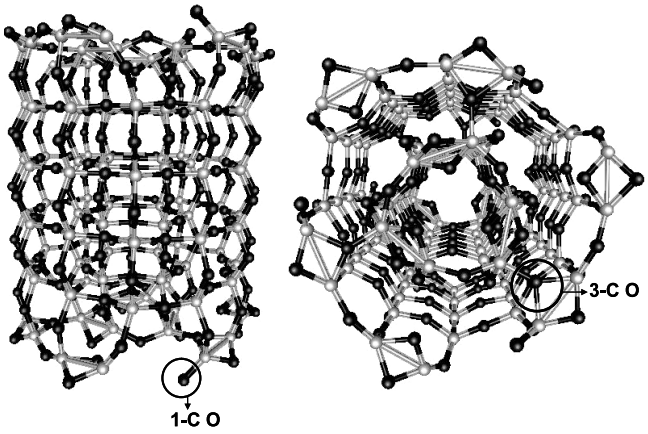

Figure 8. Side and longitudinal view of a (12–6)M MWT. One- and three-coordinated oxygens are encircled.

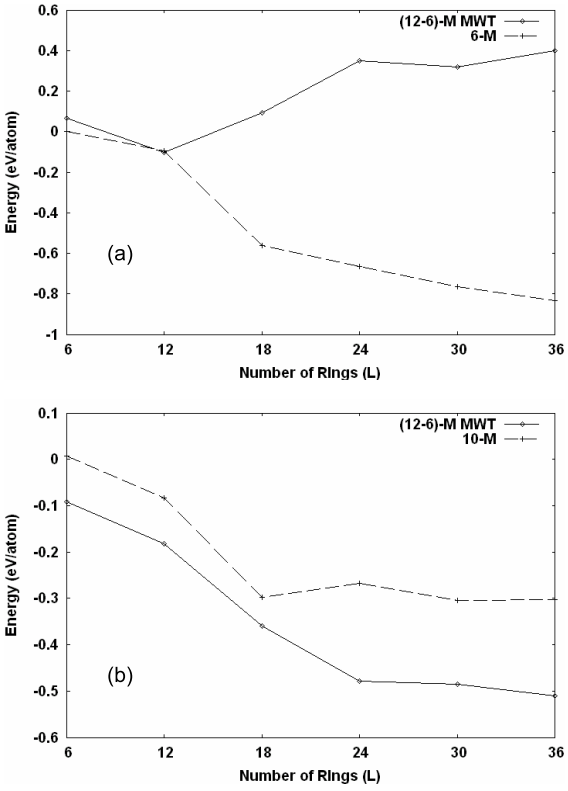

Figure 9. Variation in binding energies of the (12–6)M MWT as a function of number of rings for (a) FB and (b) BKS. For reference, in each figure, the binding energy of the most stable family of SWT (as a function of L) for the particular potential is also given. Note that the energies are expressed with respect to the $6M$–$6L$ structure.

The relative BEs of the FB and BKS (12–6)M are a study in contrast. The BKS MWT always is lower in BE than the corresponding length SWT, while the opposite is true for the FB MWT

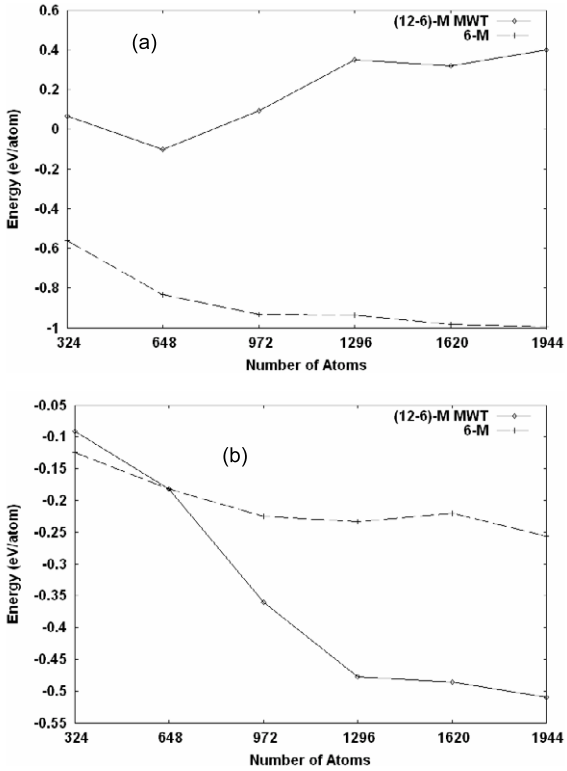

Figure 10. Variation in binding energies of the (12–6)M MWT as a function of number of atoms for (a) FB and (b) BKS. For reference, in each figure, the binding energy of the 6-M structure having the same number of atoms is also given. Energies are expressed with respect to the 6M–6L structure for the respective potentials.

beyond $L = 12$. Moreover, the FB (12–6)M has a minimum energy length at $L = 12$, while the BKS MWT has no distinct minimum in the range of L we treated. Both become weakly dependent on length above 24L. We also compared the BE of the (12–6)M MWT and 6M structures that had the same number of atoms; see figures 10(a) and (b). Again, the FB and BKS MWTs exhibit essentially opposite behaviors. Except for the smallest system (324 atoms), the BKS MWTs are more stable with respect to their 6M counterparts, while the FB 6M tubes are always more stable than the FB (12–6)M MWTs. This distinction is striking, given the common behavior that more aggregated systems are at least weakly stable with respect to their less aggregated counterparts. At least in this sense, FB clearly favors small systems. MWTs with 1296 or more atoms are essentially degenerate energetically with respect to length for either parameterization, consistent with a finite BE infinite-system limit.

The structural quantities (A1, A2, R1, R–R) of the BKS and FB MWTs at different lengths are given in figures 11(a) and (b). As might be expected from the SWTs, R1 and R–R for the FB MWTs are greater than the corresponding BKS quantities, though at large L ($\geqslant$30), the R–R values from both parameterizations become comparable. Similar to the 12M–6L twin-columnar structure, the various MWTs also involve 3-C and 1-C Os. While the 1-C oxygen atoms are present at the ends in both the MWT and the twin-columnar 12M–6L, the 3-C Os are present only at the ends of the MWT. This difference with respect to the 12M–6L structure is because in it the 3-C Os serve as connectors and are present along the length of the tube.

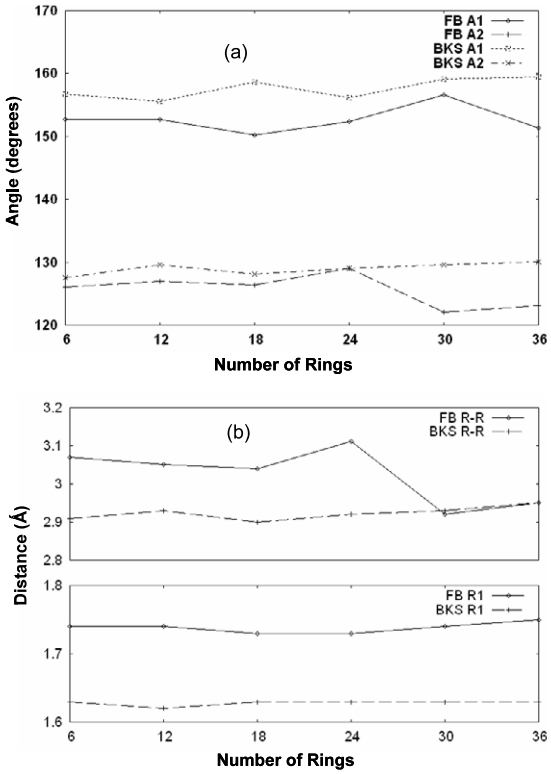

Figure 11. Variation of (a) A1 and A2, (b) R1 and R–R for FB and BKS (12–6)M MWTs.

3.3. Tensile and bending properties of silica SWTs and MWTs

We turn to the response of the nanotubes under tensile and bending strains. We used a strain rate of 5×10^{-7}/(MD time step), in order to include thermal relaxation effects fully as the material fails. The MD time step was 2 fs, hence the strain rate was 2.5×10^{-4} ps^{-1}. Each simulation ran 500 000 time steps after thermalization.

3.3.1. Tensile. When subjected to uniaxial tensile strains, the failure mechanisms of all SWTs for both EAS and PS were similar for both parameterizations. The bond breaking and material separation occurred near one of the SWT ends (at both 10 and 300 K). At first thought, such behavior might be attributed to the presence of strained end-caps. However, the failure mode was the same for both EAS and PS, so that speculation does not hold up. Instead, detailed examination of the Si–O bond distances and inter-ring distances (R–R) suggests that the nanotubes deform via initiation of a stress wave toward one end. The wave traverses the tube and ultimately leads to fracture at an end. The initial asymmetry in this process originates in the thermalization procedure which, for any given type of rod, will produce slightly different configurations (positions, velocities) depending on the precise number of MD thermalization steps. Such thermalized configurations do not preserve precisely the initial symmetry of the rod. The existence of stress waves follows from the pumping of the system caused by the application of strain (effective external force) at each MD step followed by as much relaxation (accommodation to internal forces) as is possible for each time step. We note that the effects of

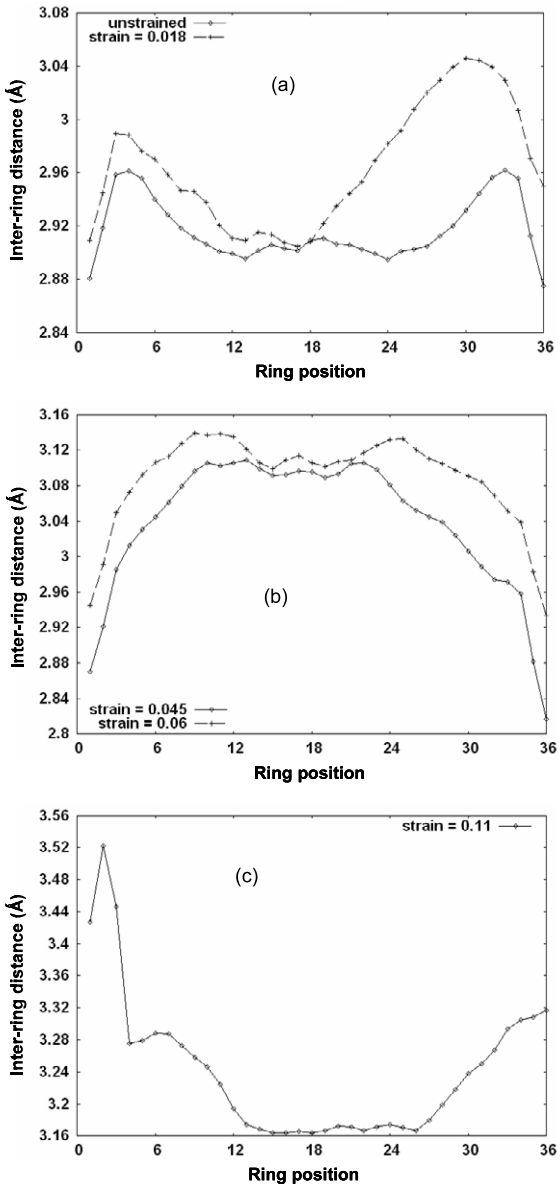

Figure 12. Variation in R–R as a function of ring position for strains of (a) 0.015, (b) 0.045 and 0.06, and (c) 0.11 for the FB 6*M*–36*L* SWT when subjected to a uniaxial strain rate of 2.5×10^{-4} ps^{-1} at 10 K.

this sort of oscillatory behavior on the relationship between stresses from atomistic simulations and from continuum systems had been discussed by Zhou [27] (at the very end of the paper), though in the context of thermal oscillations.

Insight into the failure process is aided by consideration of figures 12(a)–(c). They display the variation in R–R as a function of ring position (along the system) for different strains for the FB 6*M*–36*L* at 10 K. Assuming, for convenience, that the principle axis of the SWT

Figure 13. Fracture of the FB $6M$–$36L$ SWT when subjected to a uniaxial strain rate of 2.5×10^{-4} ps^{-1} at 10 K.

is horizontal such that the ring position index increases from left to right, we see that at strain = 0.018 (figure 12(a)) the R–R distances between ring positions 30–35 (i.e. on the right side of the SWT) are larger than the R–R values for the other ring positions. At a higher strain = 0.045 (figure 12(b)), the R–R distances are larger in the middle of the rod, while at strain = 0.060 (figure 12(b)), the R–R distances between ring positions 5–10 are now the largest. At higher strains (figure 12(c)) the R–R distances at the left end of the SWT continue to increase, and finally, the left end (usually consisting of 2–3 rings) separates as illustrated in figure 13. In short, during the initial stages of strain application, one end of the SWT is under tension (or compression) with respect to the other end, a situation that gives rise to a stress wave that propagates along the SWT as the system is subjected to increasing strain.

Figure 14(a) presents the 10 K tensile stress–strain curves of the $6M$–$36L$ SWT for both parameterizations. Clearly the stress variation in what ordinarily would be the elastic regime is highly non-linear. Indeed, within that strain range, there is an interval for which the average stress response is approximately strain independent. This behavior can be correlated to the variation in inter-ring distances (figures 12(a)–(c)) and its relation to the definition used for calculating the stress. Recall that the calculated stress is a local quantity characteristic of the end-cap forces. Specifically, the strain-independent interval corresponds to the initiation and propagation of the stress wave just discussed. In that regime, the calculated stress can be roughly constant or even decrease. The calculated virial stress exhibits the same behavior, a fact which lends confidence to the notion that the behavior is not simply a computational artifact.

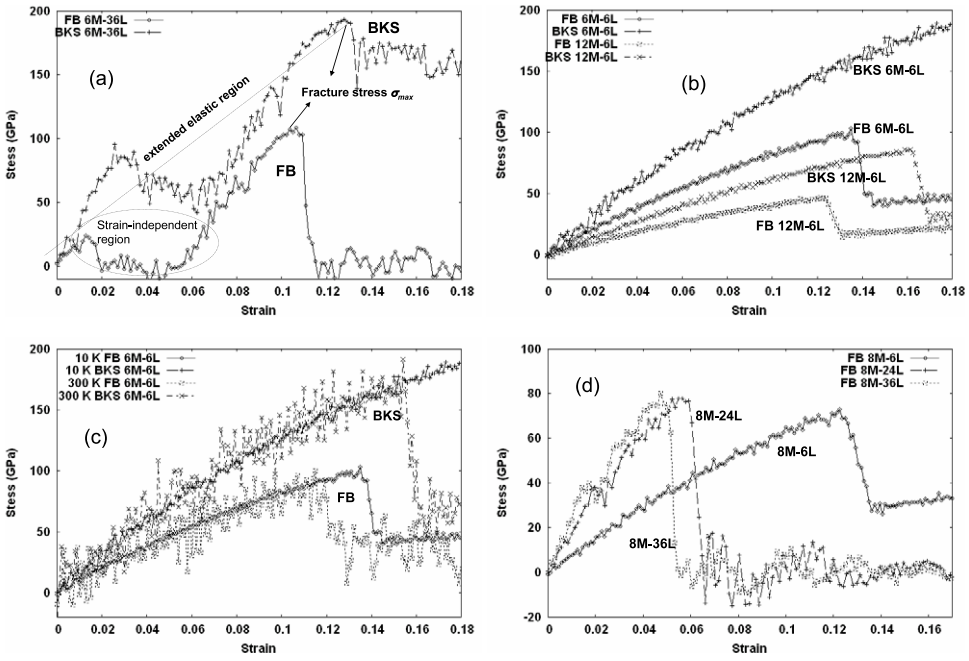

Figure 14. Uniaxial stress–strain curves for (a) 10 K FB and BKS $6M$–$36L$ SWT, (b) 10 K FB and BKS $6M$–$6L$ and $12M$–$6L$ SWT, (c) 10 and 300 K FB and BKS $6M$–$6L$, and (d) FB $8M$ SWTs for various L.

For a given M, the phenomenon of stress wave propagation is most noticeable in the longer SWTs. Consequently the strain-independent regions of the stress–strain curves for the shorter SWTs are not obvious to the unaided eye. See figure 14(b) for example. Note also that the constituent rings of the SWT remain rather well defined even as the system is strained uniaxially, hence none of the structures exhibit 'necking' prior to failure.

Values of the Young's modulus E at $T = 10$ K of the family of structures for each M are given in tables 3 and 4. We approximated E for the SWTs by evaluating the slope of the stress–strain curve in what we denote as the 'extended elastic' regime in figure 14(a), i.e., linear interpolation from zero strain to failure. Obviously the approximation is quite severe in that it ignores the nearly strain-independent stress region just discussed. The approximation clearly is better for the shorter tubes in any fixed-M family. It is important to note that the stress responses of all structures (at 10 K) until failure were independent of the initial conditions (i.e. velocity distributions and starting configuration) though the end at which failure occurred depended on the initial conditions. In other words, the variation in tensile stress maxima ($\sigma_{\max}$), strains ($s^{\max}$), and consequently E were negligible though the location of failure varied depending on the initial condition.

Tables 3 and 4 together with table 5 comprise a survey of the tensile and bending properties of the various systems. Note that the BKS $12M$-($6L$ and $12L$) moduli reported in table 3 are for the twin-columnar structures.

The following trends emerge. The values of E, tensile stress maxima ($\sigma_{\max}$), and tensile strains ($s^{\max}$) before failure of the BKS SWTs generally exceed those for the corresponding FB systems. Exceptions are E for the $8M$–18, 24, 30, $36L$ SWTs and $s^{\max}$ for the $4M$–$18L$ SWT. E is almost independent of temperature, though there are, of course, more fluctuations in the

Table 3. Young's and bending modulus (10^3 GPa) for single-walled structures as a function of number of ring members (M) and layers (L), regarding both BKS and FB parameterizations at 10 K under stretching and bending deformations. See text regarding omitted values.

		Stretching		Bending	
M	L	BKS	FB	BKS	FB
4	6	1.72	1.19	2.40	1.84
	12	1.68	0.70	2.23	1.75
	18	1.70	0.65	1.68	1.51
	24	1.23	0.90	—	—
	30	—	—	—	—
	36	—	—	—	—
6	6	1.19	0.86	2.16	1.51
	12	1.21	0.86	2.18	1.30
	18	1.22	0.86	2.19	1.01
	24	1.22	0.88	2.15	1.00
	30	1.19	0.84	2.23	1.02
	36	1.24	0.86	2.20	1.01
8	6	0.90	0.66	1.40	1.04
	12	0.89	0.73	1.59	1.04
	18	0.92	0.92	1.88	1.12
	24	1.02	1.54	1.98	1.16
	30	1.02	1.69	1.89	1.06
	36	1.02	1.76	1.96	1.05
10	6	0.71	0.53	1.10	0.64
	12	0.73	0.58	0.99	0.52
	18	0.72	0.57	0.94[a]	0.55
	24	0.73	0.57	1.46[a]	0.57
	30	0.73	0.57	1.71[a]	0.38
	36	0.73	0.47	1.64[a]	0.32
12	6	0.61[b]	0.43	0.89[b]	0.63
	12	0.63[b]	0.44	0.89[b]	0.56
	18	0.66	0.43	0.55[c]	0.51
	24	0.66	0.46	0.58[c]	0.50
	30	0.67	0.45	0.45[c]	0.45
	36	0.67	0.46	0.30[c]	0.50

[a] Change of geometry induced by bending deformation. Splitting into $2 \times 5M$ rods.
[b] Initial geometry is the $2 \times 6M$ column structure.
[c] Change of geometry induced by bending deformation. Splitting into $2 \times 6M$ rods.

stress response at $T = 300$ K. See, for example, the temperature dependence in figure 14(c) (and as well, the results discussed below in the context of full quantum force calculations). Typically, for a given M, E does not vary greatly with L. Notable exceptions again are the $8M$ FB SWTs, for which E generally increases with increasing L and jumps between $L = 18$ and 24. The variation in E with L is not nearly so dramatic for the $8M$ BKS SWTs. The other major exception is the irregular variation of E for the $4M$ SWTs in both parameterizations. This irregular behavior of the longer $4M$ structures correlates with the distorted tubular structures discussed already. Those structures make the longer $4M$ SWTs comparatively much weaker. For the other structures, failure occurred at smaller strains for increasing L. (Recall that for the $4M$s, the BKS $30L$, $36L$ and FB $24L$, $30L$, and $36L$ systems would not equilibrate to a straight geometry, so table 3 omits those systems.)

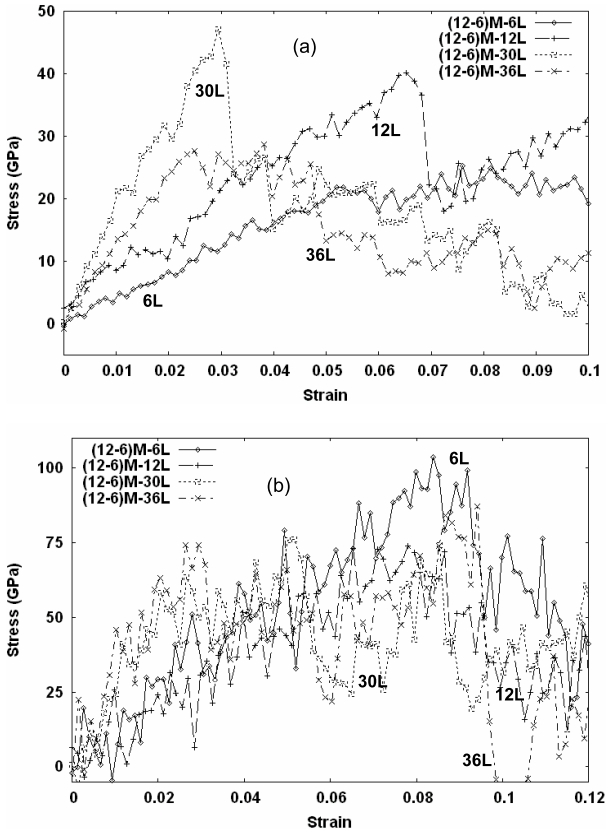

Figure 15. Uniaxial stress–strain curves for (a) FB and (b) BKS (12–6)M MWTs.

Other interesting behaviors include the fact that for a given L, E and $\sigma_{\max}$ decrease with increasing M for the BKS structures. The behavior of the FB SWTs is more varied. Putting aside the $4M$s as anomalous, the FB $12L$s have E decreasing with increasing M, but for $L > 12$ the $8M$s are quite substantial exceptions. At fixed L, $\sigma_{\max}$ for the FB structures (again excluding $4M$) generally decreases with increasing M, but for $L = 30$ and 36, $M = 12$ is an exception. The $M = 10$ FB structures are notably weaker in both cases. Note also that the $8M$ and $10M$ FB rods exhibit dramatic size effects in $s^{\max}$ between $L = 12$, 18 and $L = 24$, 30 respectively. Corresponding $\sigma_{\max}$ behavior occurs in the $10M$ FB SWTs but not the $8M$s. Whether this is a genuine size effect parameterized by FB is another open question beyond the reach of the present calculations. It is at least suggestive that BKS does not generate comparable behavior.

Turning to the MWTs under uniaxial strain, though failure also occurred at the ends, there was no evidence of stress-wave-assisted fracture akin to that seen in the SWTs. Similar to the SWTs, during the initial stages of strain application, one end was in tension relative to the other. However, with increasing strain, that end continued to be in tension, a feature which led to fracture there. See discussion above. The 10 K Young's modulus of the MWT is listed in table 4, and the MWT stress–strain curves are given figure 15. Notice that BKS predicts the (12–6)M–6L to be the stiffest of these MWTs, while FB predicts the opposite.

3.3.2. Bending. Distinct from the uniaxial stretching case, for bending the various structures did not always separate at the ends. Typically, bond breakage first occurred at the middle of

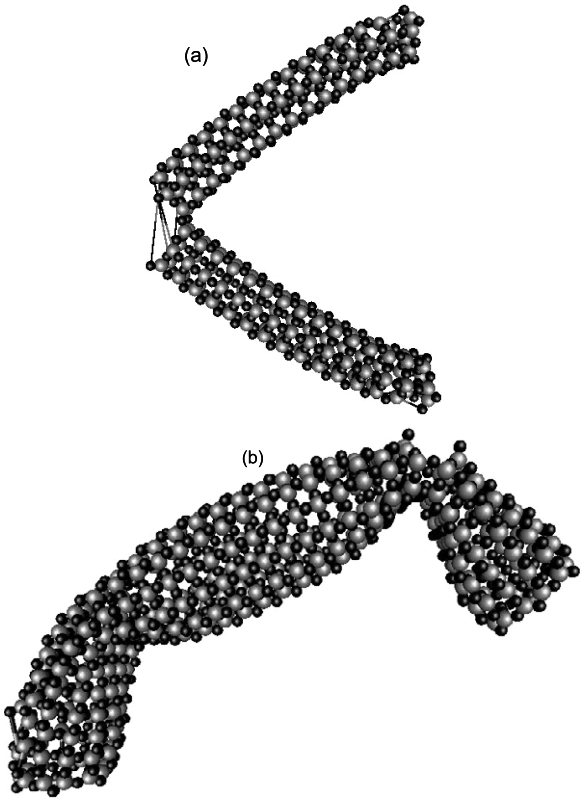

Figure 16. Fracture of (a) FB $6M$–$30L$ SWT, (b) FB $12M$–$36L$ SWT, under bending when subjected to a strain rate of 2.5×10^{-4} ps^{-1} at 10 K.

Table 4. As in table 3 for (12–6)M MWT structures.

	Stretching		Bending	
L	BKS	FB	BKS	FB
6	1.13	0.35	1.70	0.44
12	0.92	0.61	1.53	1.05
18	1.03	0.85	1.68	1.08
24	0.85	0.96	1.73	0.52
30	0.91	1.10	1.65	0.52
36	0.91	0.87	1.55	0.50

the structure in the tensile zone (i.e. outside the unstrained central axis), behavior which is entirely plausible. The smaller radii structures are much stronger and stiffer, with separation occurring at the middle of the structure (figure 16(a)), while the much weaker larger radii structures ($M > 8$) fail via necking at more than one site (figure 16(b)). Qualitatively, the smaller radii structures snap (to use an analogy with macroscopic failure) while the larger radii structures fold (or crimp). This difference in failure mode is a result of the relative stability of the respective ring structures. The $6M$ and $8M$ rings are structurally more stable under bending than the $10M$ and $12M$ rings. Further, the longer BKS $10M$ and $12M$ structures proved to be

Table 5. Comparison of maximum stress–strain points (i.e. just prior to failure), σ_{max} (GPa), s^{max}, as a function of layers (L) for various structures and for both BKS and FB parameterizations at 10 K under stretching and bending deformations.

		Stretching				Bending			
		BKS		FB		BKS		FB	
M	L	s^{max} (%)	σ_{max} (GPa)	s^{max} (%)	σ_{max} (GPa)	$s^{max}_{y^a}$ (%)	σ_{max} (GPa)	$s^{max}_{y^a}$ (%)	σ_{max} (GPa)
4	6	16.4	266	9.8	118	18.1	262	11.0	192
	12	14.7	264	14.2	83	6.1	167	15.9	54
	18	14.5	271	16.3	88	6.5	137	17.4	103
	24	12.9	266	11.1	118	—	—	—	—
	30	—	—	—	—	—	—	—	—
	36	—	—	—	—	—	—	—	—
6	6	17.8	193	13.5	103	13.1	257	13.6	201
	12	17.4	182	13.2	96	13.6	256	13.0	158
	18	14.1	190	11.0	107	11.7	240	14.3	157
	24	13.5	196	10.6	109	10.4	222	12.4	177
	30	12.9	196	11.0	110	10.8	256	12.4	156
	36	12.8	196	10.7	110	10.2	264	12.8	173
8	6	17.0	142	12.3	74	11.2	126	13.0	131
	12	14.6	133	12.1	69	10.1	144	13.2	115
	18	12.9	143	8.0	79	13.4	148	8.9	111
	24	12.5	145	5.9	79	8.3	135	6.7	111
	30	12.3	144	4.8	80	6.0	131	17.2	114
	36	11.8	145	4.7	80	5.6	142	6.4	101
10	6	16.1	105	11.8	56	17.0	108	15.0	80
	12	15.0	101	12.5	54	17.1	83	17.5	70
	18	11.7	104	10.8	53	15.0[a]	72[a]	14.0	73
	24	17.0	105	10.6	53	3.4[a]	58[a]	8.9	58
	30	16.9	103	5.2	32	14.7[a]	57[a]	6.7	37
	36	13.8	102	5.3	22	2.3[a]	45[a]	6.3	31
12	6	15.8[b]	87[b]	12.2	47	9.2[b]	66[b]	11.5	55
	12	15.2[b]	84[b]	9.9	42	17.5[b]	56[b]	8.9	44
	18	14.4	86	11.2	49	8.8[c]	48[c]	11.3	49
	24	14.3	88	10.9	49	9.2[c]	49[c]	6.4	49
	30	14.0	88	10.6	51	4.4[c]	50[c]	7.4	39
	36	14.0	87	10.4	50	4.7[c]	37[c]	8.0	43

[a] Change of geometry induced by bending deformation. Splitting into $2 \times 5M$ rods.
[b] Initial geometry is the $2 \times 6M$ column structure.
[c] Change of geometry induced by bending deformation. Splitting into $2 \times 6M$ rods.

unstable under bending. At very small bending strains (<0.05), they rearrange into the twin-columnar structures previously discussed for the $12M$–($6L$ and $12L$) SWT.

The bending stress–strain curves for selected structures for both FB and BKS parameterizations are given in figure 17 and the bending moduli B and failure data for the various structures also are tabulated in tables 3–5. Similar to the stretching results, for a given M, B does not vary much with temperature and L. Further, for a given structure, B was usually greater than E. One can rationalize the difference in moduli on the basis that the initiation and propagation of stress waves determine the stress response and nature of failure of the structures under tension, while in structures that are bent the loss of axial symmetry impedes stress wave propagation. Thus, the structures are stiffer when bent as compared to uniaxially strained. The

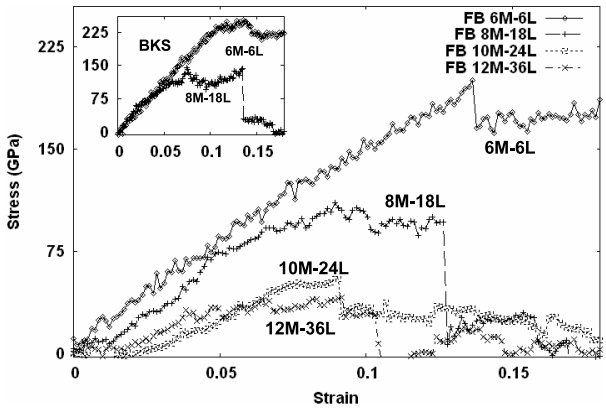

Figure 17. Bending stress–strain curves for selected FB and BKS SWT when subjected to a strain rate of 2.5×10^{-4} ps^{-1} at 10 K. The inset represents the corresponding end-cap structural quantities.

MWTs fail in similar fashion to the SWTs under bending, with initial bond breakage occurring at the middle. As expected from the SWT behavior, the BKS MWTs are much stiffer than FB; see table 4.

3.4. All quantum mechanical and multi-scale simulations

The often disparate (and sometimes peculiar) predictions of the two potential parameterizations (BKS, FB) make insights from quantum mechanical (QM) calculations of the inter-atomic forces particularly desirable. The issue is particularly important because of the exclusive parameterization of FB to quantum mechanical forces on small nanostructures of various symmetries. As sketched in section 1, we used two different approximations to treat the $6M$–$6L$ SWT for that purpose. One was full quantum (FQ) simulations in which the forces on all atoms were obtained from the approximate QM methodology called neglect of diatomic differential overlap (NDDO). Unlike the usual quantum chemistry implementation however, we used NDDO parameters obtained via the transfer Hamiltonian (TH) method of Taylor *et al* [23]. The essence of their approach is to find NDDO parameters such that the resulting forces reproduce bond-breaking forces for selected paradigmatic molecules as calculated in very high quality quantum chemical calculations. The simplicity of the TH-NDDO Hamiltonian results in a relatively affordable electronic structure calculation for each configuration of atomic positions in the MD run.

For insight into the relationship between size and QM, we also employed a multi-scale approach. In it, QM forces are computed in a small sub-region of the system with the rest of the forces from classical potentials. We used the composite nanorod system previously proposed and studied by Mallik *et al* [22]. It consists of a central QM ring, also with TH-NDDO forces. The rest of the atoms interact via a pair potential of the BKS/FB form but parameterized differently. The parameterization, NTH-2, is constrained to reproduce the equilibrium tensile elastic moduli for an all-QM (TH-NDDO) forces simulation of the $6M$–$6L$ SWT. Interactions between the classical and QM regions are handled by substituting a modified F atom (modified NDDO parameters) as a pseudo-atom at the sites of the bridging O surrounding the central ring. To identify the effects of the NTH-2 parameterization (recall table 1 for values), we also did classical MD with it.

Table 6. Comparison of stress–strain data for the FQ and classical (BKS, FB and NTH-2) treatments of the $6M$–$6L$ rod subjected to uniaxial strain (proportional strain—PS) at a rate of 0.025 ps^{-1}. The maximum stress–strain point before failure ($\sigma_{\max}$, $s^{\max}$) and Young's modulus (E) are reported.

	1 K			10 K			300 K		
	$s^{\max}$ (%)	$\sigma_{\max}$ (GPa)	$E(\times 10^3$ GPa)	$s^{\max}$ (%)	$\sigma_{\max}$ (GPa)	$E(\times 10^3$ GPa)	$s^{\max}$ (%)	$\sigma_{\max}$ (GPa)	$E(\times 10^3$ GPa)
FQ	21.3	196	1.04	21.2	197	1.04	20.1	184	1.05
BKS	18.4	189	1.39	18.0	187	1.39	15.1	173	1.40
FB	13.7	100	0.92	13.7	102	0.93	11.7	82	0.88
NTH-2	13.4	101	1.01	13.3	99	1.01	11.3	88	1.01

The FQ and multi-scale simulations were done for both tensile and bending stress response with strain rate of 0.025 ps^{-1}, 5000 time steps, each 2 fs. Compared with our all-classical work, this is a much shorter MD series with much more rapid strain, obvious consequences of the relative computational cost of the QM forces. In addition, we used the Nosé–Hoover thermostat in contrast to the velocity rescaling used in related prior work [22]. The simulations were carried out at $T = 1$, 10, and 300 K. We used both EAS and PS deformations for tensile stress and EAS for bending. Values of Young's modulus were obtained by linear regression from 0 to 5% strain for each of the simulated systems. The failure-strain, maximum stress point was determined by fitting the stress–strain data to a second- or third-order polynomial.

As shown in tables 6 and 7 (for PS and EAS respectively), we obtain a maximum stress and failure strain close to the FQ calculation for the BKS potential but for the Young modulus we find better agreement for the FB and NTH-2 potentials. Recall that NTH-2 was trained specifically to match the Young's modulus of the $6M$–$6L$ SWT NDDO-TH. Interestingly, the quantum-mechanically trained potential parameterizations, NTH-2 and FB, give rather similar results for $s^{\max}$, $\sigma_{\max}$, $s^{\max}_{y_a}$, and $\sigma_{\max,\text{bending}}$, especially at the lower temperatures. A cautionary fact is that the FB parameterization, developed and calibrated to FQ calculations on small silica systems, does not give results that agree with the present FQ results. The difference surely arises in part from the two different QM approximations used, TH-NDDO here versus DFT in the FB work. The fact that the two parameterizations nonetheless give similar results suggests that the functional form of the potential limits the extent to which QM parameterization inputs can influence the calculated behavior of nanosystems.

The bending results are shown in table 8. Relative to the FQ calculations, *all* three potential parameterizations overestimate the bending modulus B and the location of the maximum stress, failure-strain point. The BKS potential follows the same tendency as observed in stretching deformations: it gives the strongest bending modulus. All of the bending calculations, irrespective of the source of forces, exhibit a plastic zone between 12% strain and failure because of atomic reorganization in the compression zone (inside the central surface). Increasing the temperature results in a longer plastic zone for the FQ calculation that is not observed in any of the classical potential cases.

At the lower temperatures, the qualitative character of failure of the FQ $6M$–$6L$ nanorod under either tension or bending in all cases was similar to that observed using the all-classical forces. Such behavior is consistent with the $6M$–$6L$ mechanical properties under tension (recall

Table 7. As in table 6 but for end-atom strain—EAS.

	1 K		10 K		300 K	
	$s^{\max}$ (%)	$\sigma_{\max}$ (GPa)	$s^{\max}$ (%)	$\sigma_{\max}$ (GPa)	$s^{\max}$ (%)	$\sigma_{\max}$ (GPa)
	$E(\times 10^3$ GPa)		$E(\times 10^3$ GPa)		$E(\times 10^3$ GPa)	
FQ	21.8	197	21.8	198	19.4	179
	1.05		1.05		1.06	
BKS	19.8	198	19.4	195	16.6	182
	1.41		1.40		1.43	
FB	15.2	108	15.1	108	12.0	88
	0.94		0.94		0.88	
NTH-2	13.9	105	13.5	103	12.0	89
	1.02		1.02		1.01	

Table 8. As in table 6 for bending (end-atom strain—EAS) at strain rate of 0.025 ps^{-1}. The maximum stress–strain point before failure ($\sigma_{\max}$, $s_{y^a}^{\max}$) and Bending modulus (B) are reported.

	1 K		10 K		300 K	
	$s_{y^a}^{\max}$ (%)	$\sigma_{\max}$ (GPa)	$s_{y^a}^{\max}$ (%)	$\sigma_{\max}$ (GPa)	$s_{y^a}^{\max}$ (%)	$\sigma_{\max}$ (GPa)
	$B(\times 10^3$ GPa)		$B(\times 10^3$ GPa)		$B(\times 10^3$ GPa)	
FQ	11.9	128	17.8	142	12.6	112
	1.37		1.31		1.14	
BKS	13.1	199	9.8	194	10.0	198
	1.98		2.27		2.28	
FB	18.0	143	11.2	150	10.3	136
	1.18		1.51		1.50	
NTH-2	18.3	157	11.1	166	11.2	153
	1.39		1.70		1.63	

tables 6–8). At 300 K, failure was characterized by a substantial non-linear or plastic zone in the stress–strain curves and fracture was more gradual than at the lower temperatures.

Results from multi-scale treatment of stretching and bending in the composite system are shown in table 9. The bending results are close to those from the FQ calculations. Under stretching deformation, the composite treatment gives a $6M$–$6L$ Young's modulus close to that from the NTH-2 potential (which is used on the classical zone of the composite). The maximum of the tensile stress–strain curve from the multi-scale treatment is much softer than for either the full classical or FQ systems. In principle, the dependence of this softening on the size (number of rings) of the QM zone should be studied but a problem intervenes, as follows.

All multi-scale methodologies face the challenge of maintaining consistency (or, at least, minimizing inconsistency) between the QM and classical potential forces. In the present case, as the number of rings included in the quantum region is increased, the difference between the stiffness calculated from classical and QM forces becomes problematical. The difference is so large that the system becomes unstable during simple relaxation without any externally imposed stress. The result is that the nanotube symmetry is broken and there is notable atomic position reorganization in both the quantum zone and the buffer zone adjacent to it. Such behavior clearly prevents the application of the corresponding stretching and bending deformation to composite (embedded quantum zone) systems with more than one ring.

Table 9. Comparison of the stress–strain data for the FQ and multi-scale (QM-MD) simulations of the $6M$–$6L$ rod subjected to uniaxial strain and bending at strain rate of 0.025 ps^{-1} at 1 K. The maximum stress–strain point before failure and the Young's (E) and Bending (B) moduli are reported.

	Stretching		Bending	
	s^{max} (%)	σ_{max} (GPa)	$s^{max}_{y^a}$ (%)	σ_{max} (GPa)
Q. Z. (rings)	$E(\times 10^3$ GPa)		$B(\times 10^3$ GPa)	
1	16.1	95	11.3	130
	1.01		1.31	
6 (FQ)	21.8	197	11.9	128
	1.05		1.37	

4. Conclusions

We have examined the structure, energetics and mechanical properties of various cylindrical silica nanotubes as a function of length and radius using MD techniques. The inter-atomic interactions were modeled first via two different parameterizations of the same pair potential form, FB and BKS. Those parameterizations are based on distinctly different reference systems. However, the calculated nanorod behaviors do not separate neatly by parameter set. Some calculated features of the SWT nanotubes obtained using the two sets differ greatly, while other aspects are strikingly similar. Specifically, the nature of failure of the various nanotubes under tension and bending using both parameterizations is qualitatively the same. Though the moduli of the various structures obtained differ, they are comparable in magnitude. Presumably these similarities trace to the functional form of the potential.

However, there are notable differences in predicted length dependences. One example is the moduli of the FB $8M$ SWTs, which are much more dependent on L than for the BKS counterparts. Another is the difference in the predicted existence of energetically favored lengths. A systematic distinction is that, for a given length, the BKS parameters always predict the more compact (or dense) multi-wall nanotubes to be more stable, while FB parameters predict the $6M$ structures to be energetically favored.

For comparison and additional insight into some of these differences, we also studied the mechanical properties of the $6M$–$6L$ nanotube using semi-empirical QM methods as well as multi-scale methods. At lower temperatures, failure of the FQ $6M$–$6L$ nanotube under tension and bending is qualitatively similar to that from the classical potentials as are its mechanical properties under tension. At 300 K, failure was characterized by a substantial 'plastic' zone in the stress–strain curves and fracture was more gradual. Also, the composite nanotube was slightly weaker than the FQ structure and failed at a larger fracture strain. However, the difference between the present QM results and the FB potential parameterization indicate a strong dependence on method. This is a difficulty already seen in other work on the ingredients of multi-scale simulation [28].

Since not much experimental information is available on silica nanotubes, we hope that this work will help to stimulate experimental synthesis and characterization of such structures. Having experimental data could help test one of the more striking qualitative predictions, namely the BKS energetic instability toward twin-columnar forms of the initially $12M$–$6L$ and $12M$–$12L$ nanotubes. In contrast, the FB prediction is essentially isoenergetic for the two conformations, a fact which suggests a thermodynamically driven variation in conformation. Pertinent experimental data also could help resolve the differences between and among the various calculational approaches, e.g., the length dependences of the moduli discussed above.

Acknowledgments

Financial support from NSF ITR Grant DMR-0325553 is acknowledged with thanks. We thank A Mallik, D E Taylor, K Runge, and H-P Cheng for helpful discussions.

References

[1] Bromley S T 2005 *Phys. Rev. Lett.* **95** 185505
[2] Bromley S T 2004 *Nano Lett.* **4** 1427
[3] Flikkema E and Bromley S T 2004 *J. Phys. Chem.* A **108** 9638
[4] Ji Q, Iwaura R, Kogiso M, Jung J H, Yoshida K and Shimuzu T 2004 *Chem. Mater.* **16** 250
[5] Cornelissen J J L, Conner E F, Kim H-C, Lee V Y, Magibitang T, Rice P M, Volksen W, Sundberg L K and Miller R D 2003 *J. Chem. Soc. Chem. Commun.* **8** 1010
[6] Zhang M, Ciocan E, Bando Y, Wada K, Cheng L L and Pirouz P 2002 *Appl. Phys. Lett.* **80** 491
[7] Tong L, Gattass R R, Ashcom J B, He S, Lou J, Shen M, Maxwell I and Mazur E 2003 *Nature* **426** 816
[8] Chen J-F, Ding H-M, Wang J X and Shao L 2004 *Biomaterials* **25** 723
[9] Li S, Li Z and Yan Y 2003 *Adv. Mater.* **15** 1528
[10] Nemetschek T and Hofmann U 1953 *Z. Naturf.* b **8** 410
[11] Baral S and Schoen P 1993 *Chem. Mater.* **5** 145
[12] Nakamura H and Matsui Y 1995 *J. Am. Chem. Soc.* **117** 2651
[13] Satishkumar R C, Govindaraj A, Vogl E M, Basumallik L and Rao C N R 1997 *J. Mater. Res.* **12** 604
[14] Martin C R 1994 *Science* **266** 1961
[15] Zygmunt J, Krumeich F and Nesper R 2003 *Adv. Mater.* **15** 1538
[16] Zhu T, Li J, Yip S, Bartlett R J, Trickey S B and De Leeuw N 2003 *Mol. Simul.* **29** 671
[17] Flikkema E and Bromley S T 2003 *Chem. Phys. Lett.* **378** 622
[18] van Beest B W H, Kramer G J and van Santen R A 1990 *Phys. Rev. Lett.* **64** 1955
[19] Smith W and Forester T 1996 *J. Mol. Graphics* **14** 136
[20] Byrd R F, Lu P, Nocedal J and Zhu C 1995 *Sci. Comput.* **16** 1190
[21] Taylor D E, Runge K and Bartlett R J 2005 *Mol. Phys.* **103** 10
Bartlett R J, Taylor D E and Korkin A 2005 *Handbook of Materials Modeling* (Heidelberg: Springer) p 27
[22] Mallik A, Runge K, Cheng H-P and Dufty J W 2005 *Mol. Simul.* **31** 695
[23] Taylor D E, Cory M G, Bartlett R J and Thiel W 2003 *Comput. Mater. Sci.* **27** 204
[24] Thiel W 1997 *Program MNDO97 version 5.0*
[25] Torras J, Deumens E and Trickey S B 2006 *J. Comput.-Aided Mater. Des.* **13** 201
[26] Torras J, He Y, Cao C, Muralidharan K, Deumens E, Cheng H-P and Trickey S B 2007 *Comput. Phys. Commun.* **177** 265
[27] Zhou M 2003 *Proc. R. Soc.* A **459** 2347
[28] Zhu W, Taylor D E, Al-Derzi A R, Runge K, Trickey S B, Li J, Zhu T and Yip S 2006 *Comput. Mater. Sci.* **38** 340